ACS SENSORS

pubs.acs.org/acssensors

Article

Nanorings Resembling Beehives for Ultrasensitive Fluorescence Detection

Chenglong Liao,[‖] Xiaozhen Che,[‖] Yanjun Gong,[‖] Hongwei Ji, Ling Zang,* Yanke Che,* and Jincai Zhao

Cite This: *ACS Sens.* 2024, 9, 6228−6235

Read Online

ACCESS | Metrics & More | Article Recommendations | Supporting Information

ABSTRACT: In this study, we showcase the fabrication of two nanorings resembling beehives using intricately designed donor−acceptor (D-A) fluorophores. The D−A fluorophores, featuring three twisted fluorene groups on each side of the acceptor group, adopt a bent conformation that promotes the creation of a nanoring morphology upon aggregation. With porosity for maximum binding sites, high emission efficiency, and well-organized arrangements, the nanoring-based hives offer exceptional sensitivity and selectivity in the detection of organic sulfides. Particularly, nanorings formed from benzselenodiazole-containing molecules exhibit heightened sensitivity, achieving a limit of detection (LOD) of 0.2 ppb for dimethyl sulfide and 17 ppb for dimethyl disulfide. Due to its unparalleled sensitivity and selectivity, which was not achievable with previous optical sensors, this technology enables the continuous monitoring of meat spoilage in its early stages on an hourly basis. This provides crucial insights into the exact moments when freshness begins to deteriorate and how long the meat can be stored for.

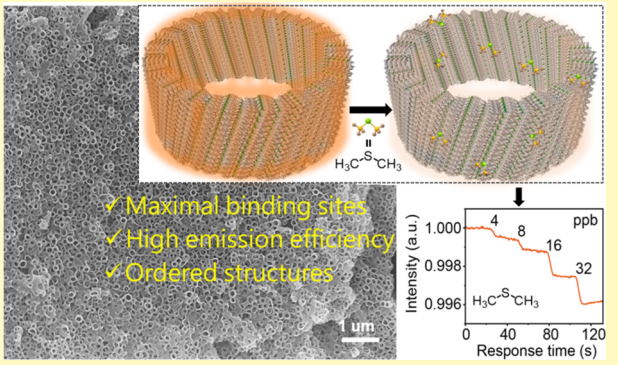

KEYWORDS: *nanorings, beehive-like superstructures, fluorescence detection, organic sulfides, meat freshness*

Porous nanostructures have sparked substantial interest because of their distinct pore-related properties, offering numerous opportunities for applications.[1−14] The self-assembly of fluorescence sensing molecules into porous nanostructures is anticipated to enhance sensitivity by maximizing binding sites and facilitating mass transfer. However, fluorophores usually possess a π-conjugated structure, causing them to form solid aggregates through π-interactions. Fluorescence sensors utilizing these solid aggregates often suffer from drawbacks such as moderate fluorescence emission,[8−14] limited active sites, and poor mass transfer, resulting in decreased sensitivity in signal responses. An alternative strategy entails employing fluorophores featuring aggregation-induced emission (AIE) attributes as foundational elements.[15−25] However, porous materials based on AIE usually exhibit only moderate emission efficiency, which greatly restricts the development of high-performance fluorescence-quenching sensors with signal amplification capabilities.[19,21−23]

The utilization of donor−acceptor (D-A) fluorophores with a twisted rigid molecular structure may provide a viable solution to the above limitations. First, D−A fluorophores demonstrate high emission efficiency in both solution and the solid state.[26] Second, they exhibit strong dipole−dipole interactions and some degree of π-coupling in ordered structures, potentially promoting exciton migration by surmounting reorganization energy barriers.[27,28] Third, by selecting different donor (D) or acceptor (A) moieties while preserving the molecular scaffold, it becomes feasible to finely tune the physicochemical properties of D−A fluorophores to enhance sensor sensitivity. Once self-assembled into porous nanostructures, these characteristics are anticipated to position D−A fluorophores as promising novel fluorescence-quenching sensors with excellent sensitivity and selectivity. Nevertheless, a strategic approach to the fabrication of D−A fluorophore-based porous nanostructures for highly sensitive detection purposes is still absent.

In this study, we report the development of two bent-shaped D−A fluorophores **1** and **2** (Figure 1a), each featuring three twisted fluorene groups on each side of the acceptor group (the benzothiadiazole or benzoselenadiazole group). The bent molecular structures induce macroscopic curvature upon aggregation, leading to the formation of two closely resembling nanorings. The nanorings further form beehive-like superstructures, showcasing high emission efficiency, porosity for maximum binding sites, and well-organized arrangements. These attributes make them ideal candidates for the sensitive detection of organic sulfides through fluorescence-quenching

Received: August 15, 2024
Revised: October 11, 2024
Accepted: October 30, 2024
Published: November 6, 2024

https://doi.org/10.1021/acssensors.4c02133
ACS Sens. 2024, 9, 6228−6235

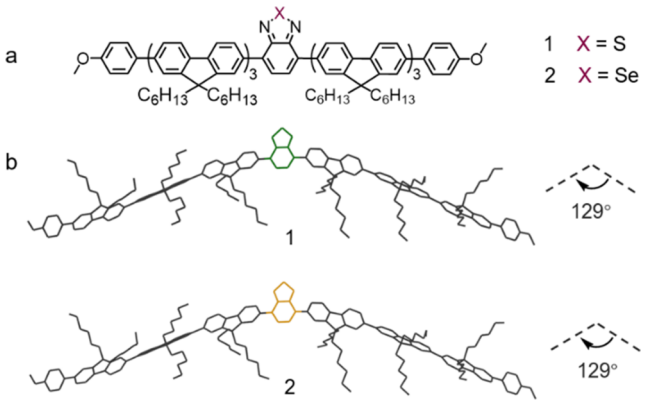

Figure 1. (a) Molecular structures of D−A fluorophores **1** and **2**. (b) DFT calculated optimal molecular conformations of fluorophores **1** and **2**.

sensing. Particularly, nanorings made from fluorophore **2** can achieve a limit of detection (LOD) as low as 0.2 ppb for dimethyl sulfide. In addition to their exceptional sensitivity, the nanoring-based hives demonstrate outerstanding selectivity toward organic sulfides, effectively distinguishing them from common interferences like moisture and various organic solvents. The nanorings' capabilities make them well suited for the continuous monitoring of meat spoilage in its very early stages on an hourly basis, revealing the exact moments when freshness begins to deteriorate and how long the meat can be stored for.

EXPERIMENTAL SECTION

Synthesis and Self-Assembly of Fluorophores 1 and 2. The synthesis route and characterization of fluorophores 1 and 2 can be found in the Supporting Information (Figures S1−S12). The formation of nanorings from either fluorophore 1 or 2 involved injecting 0.2 mL of a chloroform solution containing 1 or 2 (0.1 mg/mL) into 1 mL of acetonitrile in a 4 mL vial. The resulting solution was then left to age at 22 °C for 5 h.

Structure and Optical Characterization. Fluorescence-mode optical microscopic images were obtained by using an Olympus IX71 inverted fluorescence microscope. Scanning electron microscopy (SEM) images were recorded by using a Hitachi S-8010 microscope. Cryo-SEM images were recorded on a Hitachi S-4700 cold field emission gun scanning electron microscope equipped with a Nitrogen slush freezer and a transfer system (Leica EM HPM100). The solution samples were frozen by dropping them into a frozen sample holder and submerging them in liquid nitrogen for quick freezing. After being frozen, the sample holder was transferred to the EM ACE600 sputtering instrument for conductive spraying. Selected area electron diffraction (SAED) patterns were acquired by using a JEOL 2100 electron microscope with an electron beam energy of 120 kV. UV−vis absorption spectra were obtained by using a UV−visible microscope from CRAIC Technologies, Inc. Fluorescence spectra were recorded on a Hitachi F-7000 fluorometer. Fluorescence quantum yields of the nanorings were measured using a Hamamatsu Absolute PL Quantum Yield C11247 spectrometer coupled with an integrating sphere. The fluorescence lifetime was measured by using a time-resolved (TR) photoluminescence instrument (LifeSpec II, Edinburgh Instruments). Powder X-ray diffraction (XRD) measurements were performed on a PAN alytical X'Pert PRO instrument (40 kV, 200 mA). Powder 2D XRD measurements were conducted on a Rigaku S/Max 3000 instrument (40 keV, 30 mA).

Fluorescence Sensing. Fluorescence sensing of organic sulfide (dimethyl sulfide and dimethyl disulfide) and other interferents was performed using a custom-made device consisting of a sensory quartz tube and an ultrasensitive silicon diode detector (Figure S13). After the sensory quartz tube was loaded with 30 μL of a nanoring solution in a mixture of chloroform and acetonitrile (0.02 mM), the tube, which had dimensions of 2.5 cm in length, 0.5 mm in external diameter, and 0.1 mm in inner diameter, was emptied of solvent using a capillary. Subsequently, the sensory quartz tube, now adorned with nanorings on its inner surface, was dried by using a blower. By following the procedure, a sensory quartz tube was created, which contained nanorings assembled from both fluorophore 2 and fluorophore 1. This tube was then tested for its fluorescence responses to organic sulfides and other potential interferents in the gas phase at different concentrations. The process of creating different concentrations of gaseous dimethyl sulfides involved sealing a 20 mL jar with 0.5 mL of dimethyl sulfide overnight to saturate the vapor. To achieve varying concentrations, a small volume of saturated vapor was injected into a sealed 20 mL vial. The diluted vapor was then drawn into the sensory quartz tube by using an air pump operating at 150 mL/min for the sensing test. The diluted vapors of dimethyl disulfide as well as interferents at different concentrations were generated using the same procedure.

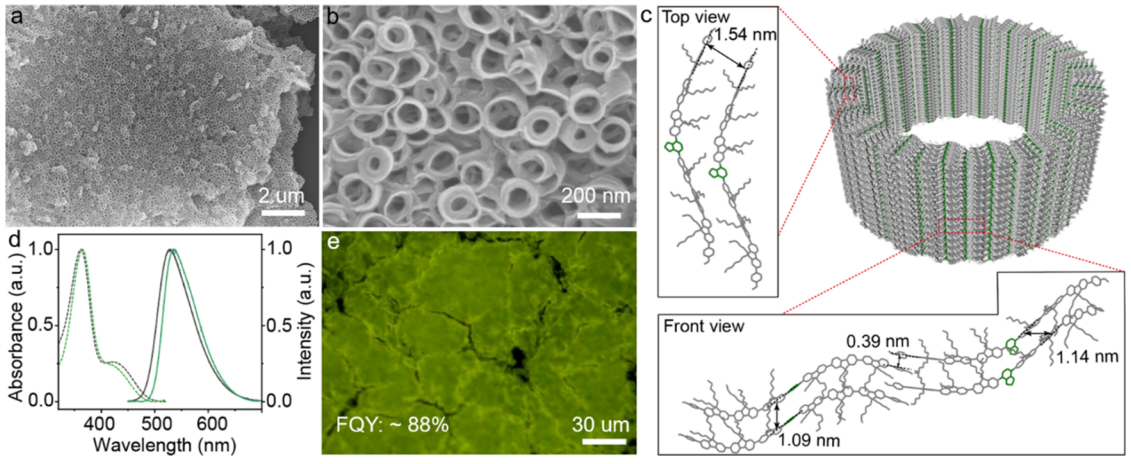

Figure 2. (a) SEM image of the beehive-like superstructure comprising nanorings formed by fluorophore **1**. (b) Magnified SEM image of the nanorings. (c) Schematic diagram of the molecular packing of fluorophore **1** in the nanorings. (d) Absorption (dashed) and fluorescence spectra (solid) of fluorophore **1** (0.09 mg/mL) in toluene (black) and nanorings placed on a glass slide (green). (e) Fluorescence-mode optical microscopic image of the highly porous multilayer film comprising nanorings formed from fluorophore **1**.

https://doi.org/10.1021/acssensors.4c02133
ACS Sens. 2024, 9, 6228−6235

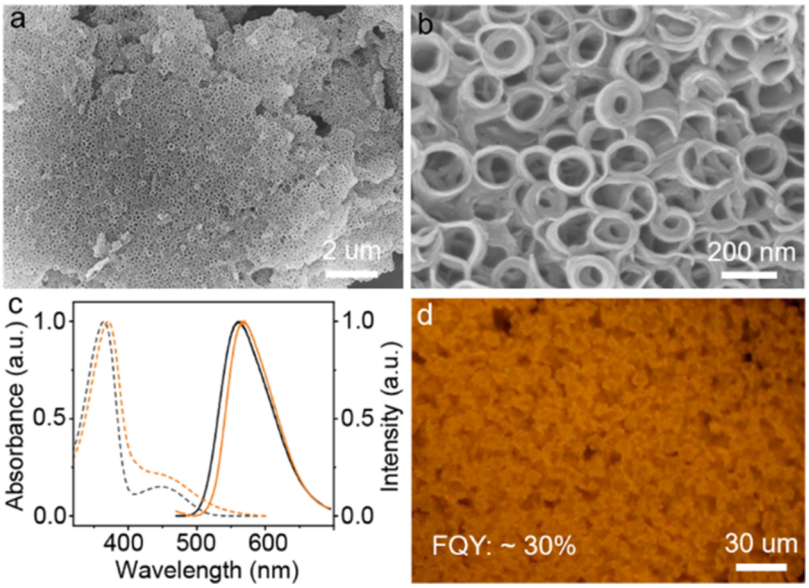

Figure 3. (a) SEM image of the beehive-like superstructure comprising nanorings formed by fluorophore **2**. (b) Magnified SEM image of the nanorings. (c) Absorption (dashed) and fluorescence spectra (solid) of fluorophore **2** (0.09 mg/mL) in toluene (black) and the nanorings placed on a glass slide (red). (d) Fluorescence-mode optical microscopic image of the highly porous multilayer film comprising nanorings formed from fluorophore **2**.

RESULTS AND DISCUSSION

The design of bent-shaped D−A fluorophores **1** and **2**, featuring three fluorene groups on each side of the acceptor group (Figure 1a), was based on the following considerations. First, the multiple D groups on each side of the A group can enhance intermolecular interactions (e.g., hydrophobic interactions between long alkyl chains), thereby promoting the formation of long-range ordered structures. Second, the increased fluorene units in fluorophore **1** promote a bent molecular conformation, as depicted in Figure 1b. The bent-shaped conformation enables the introduction of curvature upon aggregation, leading to the formation of a porous tubular structure.[4,29] Third, the A groups in fluorophores **1** and **2**, specifically the benzothiadiazole and benzoselenadiazole groups, exhibit distinct chemical properties, allowing for the adjustment of molecular electronic and optical characteristics while preserving the molecular scaffold and packing configuration.

The self-assembly of fluorophore **1** was carried out by injecting 0.2 mL of a chloroform solution of **1** (0.1 mg/mL) into 1 mL of acetonitrile in a 4 mL vial. The resulting solution was then aged at 22 °C for 5 h. SEM imaging revealed the formation of ring-like structures with outer wall diameters of approximately 150 nm (Figure 2a,b). TEM further showed that the wall thicknesses of the formed nanorings varied from 10 to 40 nm (Figure S14). Notably, the nanorings formed a closely packed aggregation, resembling a beehive superstructure, and were vertically positioned on a substrate (Figure 2a). To make sure that the nanorings were formed in solution and not spontaneously when dried, we employed Cryo-SEM to directly visualize the morphology of the aggregates formed in solution. Figure S15 displays beehive superstructures that closely resemble those seen in Figure 2a, providing further evidence of the self-assembly of nanorings in solution. The formation of the beehive superstructure is attributed to the clustering of hydrophobic long alkyl side chains between bent-shaped fluorophore **1**, which is facilitated by polar acetonitrile. The clustering is expected to be interrupted by adding hexane, which has competitive hydrophobic interactions with the long alkyl side chains of fluorophore **1**. Indeed, the introduction of hexane led to the disassembly of the beehive superstructures into dispersed nanorings in solution. These observations underscore the significance of solvophobic interactions of fluorophore **1** in polar acetonitrile in the development of the beehive-like superstructures. In addition, we used hexane instead of acetonitrile for the self-assembly of fluorophore **1**. Due to the initial involvement of the interactions between hexane and the long alkyl side chains of fluorophore **1** in the self-assembly, distinct nonuniform microsheets were formed, as shown in Figure S16. The powder XRD analysis showed that these microsheets exhibited a different molecular packing compared to the nanorings (Figure S17), emphasizing again the crucial role of polar acetonitrile in the nanorings' formation.

To gain more detailed information on the molecular packing of bent-shaped fluorophore **1**, we performed powder and two-dimensional (2D) XRD analysis of the nanorings. The *d*-spacing of 1.09 and 0.39 nm in powder XRD patterns (Figure S18) corresponds to the intermolecular distance along the ring width and π-stacking of the end groups, respectively (Figure 2c). In comparison to the powder XRD results, the 2D XRD patterns exhibited a prominent peak at 6°, corresponding to a *d*-spacing of 1.54 nm (Figure S19). This distinct peak observed in the vertically aligned nanorings can be attributed to the intermolecular distance within the wall thickness (Figure 2c). Selected area electron diffraction of a single ring (tubule) revealed *d*-spacings of 1.09 nm perpendicular to the long axis and 1.14 nm parallel to it (Figure S20), corresponding to the intermolecular distances along these two directions. The data together provide insight into the molecular arrangement of fluorophore **1** within the nanorings, as illustrated in Figure 2c. Within this packing diagram, the ordered nanorings of bent-shaped fluorophore **1** are constructed by the hydrophobic interactions of the long alkyl chains and the π-interactions of

https://doi.org/10.1021/acssensors.4c02133
ACS Sens. 2024, 9, 6228−6235

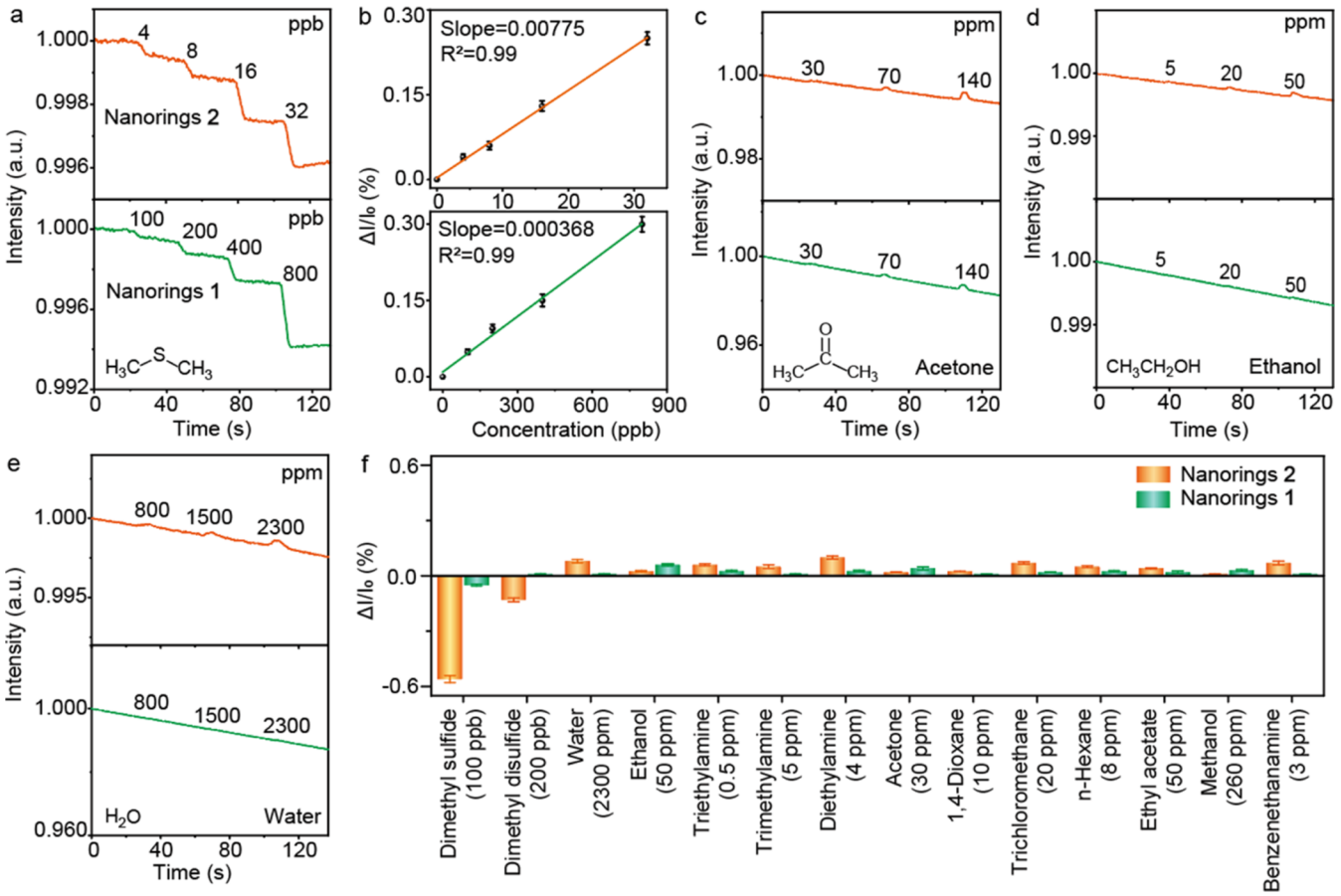

Figure 4. Fluorescence responses of the nanoring-based hives formed from fluorophore **2** (orange) and those formed from fluorophore **1** (green) to dimethyl sulfide (a), acetone (c), ethanol (d), and water (e) at different vapor concentrations. (b) Fitted fluorescence-quenching efficiency of the two nanoring-based hives upon exposure to different concentrations of gaseous dimethyl sulfide. $\Delta I/I_0$ represents the change in fluorescence intensity. The error bars represent the standard deviation of five measurements. (f) Columnar comparison of the fluorescence responses of the two nanoring-based hives upon exposure to dimethyl sulfide, dimethyl disulfide, and various potential interferents at concentrations significantly higher than those of the target sulfides. The error bars represent the standard deviation of five measurements.

the end groups. Notably, the helical packing can extend inward within the nanorings, giving rise to varying wall thickness. Despite the formation of ordered structures, the twisted molecular backbone gives rise to a weak electronic coupling between fluorophore **1**. Figure 2d shows that the absorption and fluorescence spectra of nanorings of fluorophore **1** were slightly red-shifted (less than 10 nm) in comparison with those of individual molecules of **1**. The weak electronic coupling results in a high emission efficiency of the nanorings of **1**, with a fluorescence quantum yield of approximately 88%, as depicted in Figure 2e.

Fluorophore **2**, like fluorophore **1**, produced nanorings of comparable geometry and size under identical self-assembly conditions. Figure 3a,b depicts nanorings formed from **2** with outer wall diameters of approximately 150 nm, exhibiting variations in wall thickness. Powder and 2D XRD analyses of the nanorings revealed patterns resembling those formed from fluorophore **1** (Figures S21 and S22), implying that fluorophore **2** adopted the same molecular organization as fluorophore **1**. This result is consistent with the same molecular conformation of the two molecules, as depicted in Figure 1b. Similarly, there is weak electronic coupling between fluorophore **2** in nanorings as evidenced by the fact that the absorption and fluorescence spectra of the nanorings were only slightly red-shifted compared to those of individual molecules (Figure 3c). The introduction of a benzoselenadiazole group with enhanced electron-accepting capability did not alter the molecular packing, yet it led to noticeable differences in the optical characteristics of the nanorings produced by fluorophore **2**. As depicted in Figures 3c and 2d, a considerable red shift was observed in the absorption and fluorescence spectra of the nanorings of fluorophore **2** in comparison to those of fluorophore **1** (Figure 2d). Specifically, there is a shift in the charge-transfer absorption wavelength from 435 to 455 nm and a corresponding shift in the fluorescence maximum from 535 to 569 nm. Moreover, the emission efficiency of the nanorings formed by fluorophore **2** decreased to around 30% (Figure 3d), significantly lower than that (88%) of the nanorings formed from fluorophore **1** (Figure 2e). This difference is likely attributed to increased dipole−dipole interactions between adjacent molecules and the heavy atom effect in fluorophore **2**, which could amply the nonradiative pathways of the fluorophores.[30,31]

Having obtained the two nanoring-based hives with high porosity, high emission efficiency, and distinct optical and electronic properties from different A groups, we next utilized them to construct a two-membered sensor array for detecting organic sulfides. Organic sulfides, such as dimethyl sulfide and dimethyl disulfide, are produced by microbial metabolism during meat spoilage or wound infection. These organic

https://doi.org/10.1021/acssensors.4c02133
ACS Sens. 2024, 9, 6228−6235

sulfides can be emitted readily due to their high volatility and weak binding affinity with the other components in meats, such as water and proteins. This differs significantly from the case for amines, which can readily form hydrogen bonds with amino acids or water, making them less prone to emission. Therefore, the detection of gaseous organic sulfides signifies a novel approach to evaluating meat freshness or spoilage, especially given its swiftness and precision compared to the current prevailing methods relying on the detection of amines.[32−43] Nonetheless, the assessment of meat freshness through the fluorescence detection of gaseous organic sulfides at trace levels remains rare and challenging. Recently, we utilized two D−A fluorophores for the detection of organic sulfides and monitoring meat spoilage stages.[44] However, the particles that form from these fluorophores do not possess the requisite high porosity for effective mass transfer and adsorption on the binding sites. The particles can detect dimethyl sulfide only at subppm levels in real-world scenarios. Moreover, the particles cannot detect dimethyl disulfide (another common biomarker for meat spoilage and wound infection). Consequently, the limited sensitivity to organic sulfide poses a significant obstacle in the ongoing surveillance of meat decay during its initial phases, thereby restricting its practical uses. Here, the application of nanoring-based hives is expected to address these sensitivity challenges. Figure 4a shows the fluorescence responses of the sensor array to dimethyl sulfide at trace levels, which were monitored by a device with a silicon diode detector (Figure S13). Impressively, the nanoring-based hive formed from fluorophore **2** demonstrated remarkable fluorescence quenching when exposed to dimethyl sulfide at a concentration of 4 ppb, as depicted in Figure 4a. In stark contrast, a nanoring-based hive formed from fluorophore **1** displayed significantly lower sensitivity, with a difference of 2 orders of magnitude (Figure 4a). Despite this, the detection sensitivity of nanorings formed from fluorophore **1** surpasses the previously reported best outcomes from our lab.[44] The enhanced sensitivity of the nanorings formed from fluorophore **2** is ascribed to the stronger chalcogen bonding between the benzoselenadiazole group and dimethyl sulfide, which allows for the effective trapping of dimethyl sulfide and subsequently triggers sensitive fluorescence-quenching responses. Given that the chalcogen bonding would lead to the formation of a ground-state complex between organic sulfides and fluorophores **1**-**2**, the fluorescence quenching observed above is anticipated to have no influence on the fluorescence lifetime of fluorophores **1**-**2**. Indeed, the fluorescence lifetime of the two nanoring-based hives stayed the same regardless of their exposure to different concentrations of dimethyl sulfide (Figure S23) Furthermore, the fluorescence lifetime of both fluorophores in solution was examined before and after the introduction of different concentrations of organic sulfides. Likewise, the fluorescence lifetime showed no change (Figure S24). On the other hand, the fluorescence intensities dependent on varying concentrations of dimethyl sulfide show a good fit with the Stern−Volmer plot (Figure S25). These observations indicate a static quenching mechanism via the formation of a stable complex between organic sulfides and fluorophores in the ground state. It should also be noted that the binding constant between fluorophore **2** and dimethyl sulfide is 1 order of magnitude larger than that between fluorophore **1** and dimethyl sulfide. This is in line with the significantly higher sensitivity of the nanorings formed from fluorophore **2**.

Based on the fluorescence-quenching efficiency ($\Delta I/I_0$) of the two nanoring-based hives in relation to dimethyl sulfide concentrations, a linear relationship can be established, as depicted in Figure 4b. By defining three times the standard deviation of measurement as the detectable signal and using the linear relationship obtained in Figure 4b, the LOD was calculated to be 0.2 ppb for the nanoring-based hive formed from fluorophore **2**, and 5 ppb for the nanoring-based hive formed from fluorophore **1** (Figure S26). Of note, the nanoring-based hive formed from fluorophore **2** also exhibited effective detection of dimethyl disulfide, with an LOD of 17 ppb. In contrast, the nanoring-based hive formed from fluorophore **1** showed no responses to dimethyl disulfide in identical experimental conditions (Figure S27). It is worth noting that the detection of dimethyl disulfide remains a formidable task for fluorescence sensors, possibly due to its low binding affinity for sensing materials. The notably low LOD, particularly noticeable in the nanoring-based hive formed from fluorophore **2**, along with the rapid fluorescence-quenching response of these nanorings to dimethyl sulfide (approximately 4 s, as illustrated in Figure S28), position the unique nanomaterials advantageous for practical applications in real-time assessment of meat freshness.

Next, we evaluated the fluorescence responses of the nanoring-based hives formed from fluorophores **1** and **2** toward water, amines, and various VOCs that are typically released during the process of meat spoilage and could potentially interfere with the sensor performance. As demonstrated in Figures 4c−e and S29, both nanoring-based hives displayed enhanced and reversible responses to the potential interferents at higher concentrations. The enhanced and reversible responses are likely caused by the swelling of nanorings upon encapsulation with the interferents, which can temporarily decrease intermolecular interactions, thereby increasing the emission of the molecular aggregate. A similar swelling mechanism has been observed in polymer systems as well.[45] Due to the rapid and reversible nature, the positive responses triggered by interferents do not mask the irreversible quenching responses from organic sulfides when mixed together with the interferents. Additionally, we assessed the fluorescence responses of the nanoring-based hives formed from fluorophores **2** under different temperature conditions (25 and 60 °C). The results show that changes in temperature have a minimal impact on the nanorings' ability to detect organic sulfides (Figure S30). Figure 4f presents a summary of the responses of both nanoring-based hives to dimethyl sulfide compared to different interferents, highlighting the nanorings' high selectivity toward organic sulfides over various interferents. The exceptional sensitivity and selectivity demonstrated above, coupled with the inherent advantages of affordability, simplicity, and portability associated with fluorescence sensors, would offer superior sensing capabilities in real-world scenarios compared to other detection techniques like gas-chromatography−mass spectrometry and chemiresistive sensors.[42,43] These techniques often have one or more drawbacks such as cumbersome instrumentation operation, high cost, lack of portability, and low sensitivity.[42,43]

With their markedly improved sensitivity, the nanoring-based hives could enable hourly monitoring of meat freshness, providing accurate timing of spoilage. To validate this, the sensor array, comprising two nanoring-based hives, was exposed to time-dependent volatiles emitted from four meat varieties (shrimp, fish, chicken, and pork). Prior to volatile

https://doi.org/10.1021/acssensors.4c02133
ACS Sens. 2024, 9, 6228−6235

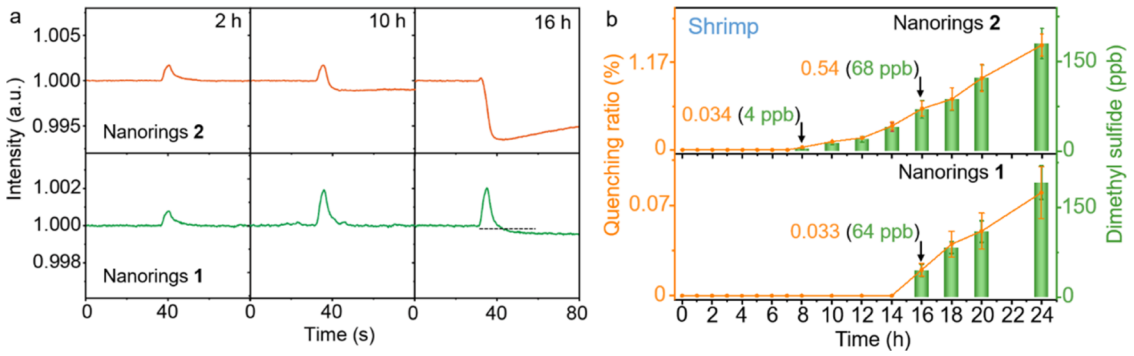

Figure 5. (a) Fluorescence responses of the two nanoring-based hives to the volatiles collected over 1 min from 5 g of shrimp meat that was stored at 18−20 °C for various durations. (d) Fluorescence-quenching ratios ($\Delta I/I_0$) of the two nanoring-based hives when exposed to the volatiles collected over 1 min from 5 g of shrimp meat that were stored at 18−20 °C for hourly durations, which corresponds to the calculated concentrations of dimethyl sulfide contained in the emitted volatiles.

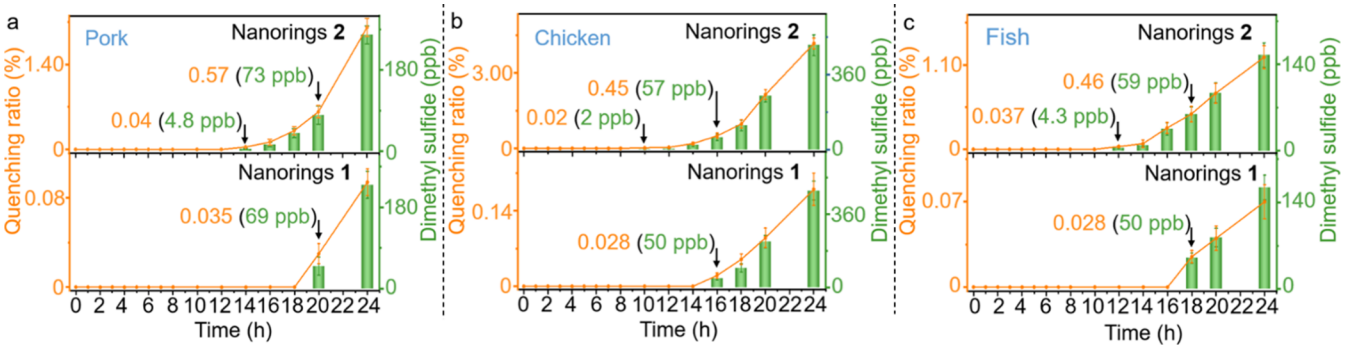

Figure 6. (a−c) Fluorescence-quenching ratios ($\Delta I/I_0$) of the two nanoring-based hives when exposed to the volatiles collected over 1 min from 5 g of pork (a), chicken (b), and fish (c) meat that were stored at room temperature for hourly durations, which corresponds to the calculated concentrations of dimethyl sulfide contained in the emitted volatiles.

collection, 5 g of meat was placed in a vial exposed to ambient conditions (temperature: 18−20 °C; humidity: 30−35%) for a set duration. Subsequently, the volatiles were collected by sealing the vial containing the meat for 1 min. Figures 5a−c show the typical fluorescence responses to the time-dependent volatiles emitted from shrimp meat. Specifically, the two nanoring-based hives exhibited enhanced responses rather than quenching reactions when exposed to the volatiles released from freshly prepared shrimp meat (Figure 5a). The results indicate that volatile compounds released from freshly prepared fish samples contain minimal levels of methyl sulfide. When exposed to the volatiles released from shrimp meat aged for 10 h, nanorings formed from fluorophore **2** initially showed an increase in response, followed by fluorescence quenching (Figure 5a). In contrast, the nanoring-based hive formed from fluorophore **1** continued to exhibit a reversible enhanced response to the same volatiles (Figure 5b), attributed to their reduced sensitivity to dimethyl sulfide. Based on the standard curves provided in Figure 4b and assuming that the quenching responses were exclusively attributed to dimethyl sulfide, the calculated concentration of dimethyl sulfide emitted from shrimp meat aged for 10 h is 16 ppb. This result is consistent with the outcome obtained from PTR ToF-MS,[44] albeit with a small margin of error. After 16 h of shrimp meat spoilage, the released volatiles caused discernible fluorescence quenching of the nanoring-based hive formed from fluorophore **1** (Figure 5a). As expected, the same volatiles triggered more substantial fluorescence quenching in the nanoring-based hive formed from fluorophore **2**, which exhibits higher sensitivity to dimethyl sulfide. By utilizing the individual standard curves as depicted in Figure 4b, the concentrations of dimethyl sulfide released from 24 h aged shrimp were calculated to be 187 and 199 ppb from the testing results of nanorings of **1** and **2**, respectively. Once again these concentration values align well with the results obtained from PTR ToF-MS analysis.[44] More fluorescence responses to volatiles released from shrimp meat on an hourly basis are presented in Figure S31. The relationship between the fluorescence-quenching ratio ($\Delta I/I_0$) and the concentrations of dimethyl sulfide released hourly is illustrated in Figure 5d. The results decisively pinpoint two critical time points (i.e., 8 and 16 h) for shrimp meat spoilage under regular ambient conditions. At the specified time points, either the nanoring-based hive formed from fluorophore **2** alone or both nanoring-based hives exhibited significant quenching responses, correlating to approximately 4 and 68 ppb of dimethyl sulfide in the vapor collected within 1 min over 5 g of shrimp. These time points mark two significant transitions in the freshness stage, thereby being pivotal for freshness assessment. Furthermore, the quenching ratios in Figure 5d allow for the estimation of shrimp shelf life under normal conditions, providing crucial data for freshness evaluation.

Analogous to the case of shrimp, the two nanoring-based hives enabled the hourly monitoring of the freshness of other meats, providing accurate timing of spoilage (Figures 6a−c and S32−S34). Based on the relationship between the fluorescence-quenching ratio and the estimated concentrations of dimethyl sulfide as a function of the storage duration of meat

https://doi.org/10.1021/acssensors.4c02133
ACS Sens. 2024, 9, 6228−6235

samples, the difference of two transition time points was observed for different meat samples (Figure 6). These data clearly indicate the spoilage difference of different meat. Likewise, the estimated concentrations of dimethyl sulfide released at 10 and 24 h for pork, chicken, and fish align with the results obtained from PTR ToF-MS analysis.[44] This supports the reliability of our sensor array for the ultrasensitive detection of organic sulfides.

CONCLUSIONS

In conclusion, we have successfully fabricated two nanorings with high emission efficiency, porosity for maximum binding sites, and organized structures by employing two bent-shaped D−A fluorophores. Each fluorophore comprises three twisted fluorene groups flanking the acceptor group (benzothiadiazole or benzoselenadiazole group), resulting in a bent conformation that promotes the creation of a nanoring morphology during aggregation. The nanorings can assemble closely adjacent to one another to form beehive-like superstructures. The nanoring-based hives exhibit exceptional sensitivity and specificity in detecting organic sulfides, including dimethyl disulfide, a compound that has not been previously identified. This information, previously unattainable with optical sensors, is crucial for practical evaluations of meat freshness and accelerates the identification of quality deterioration.

ASSOCIATED CONTENT

Supporting Information

The Supporting Information is available free of charge at https://pubs.acs.org/doi/10.1021/acssensors.4c02133.

Experimental procedures and additional data (PDF)

AUTHOR INFORMATION

Corresponding Authors

Ling Zang − *Nano Institute of Utah, and Department of Materials Science and Engineering, University of Utah, Salt Lake City, Utah 84112, United States;* orcid.org/0000-0002-4299-0992; Email: lzang@eng.utah.edu

Yanke Che − *Key Laboratory of Photochemistry, CAS Research/Education Center for Excellence in Molecular Sciences, Institute of Chemistry, Chinese Academy of Sciences, Beijing 100190, China; University of Chinese Academy of Sciences, Beijing 100049, China;* orcid.org/0000-0002-9671-3704; Email: ykche@iccas.ac.cn

Authors

Chenglong Liao − *Key Laboratory of Photochemistry, CAS Research/Education Center for Excellence in Molecular Sciences, Institute of Chemistry, Chinese Academy of Sciences, Beijing 100190, China; University of Chinese Academy of Sciences, Beijing 100049, China*

Xiaozhen Che − *Key Laboratory of Photochemistry, CAS Research/Education Center for Excellence in Molecular Sciences, Institute of Chemistry, Chinese Academy of Sciences, Beijing 100190, China; University of Chinese Academy of Sciences, Beijing 100049, China*

Yanjun Gong − *Key Laboratory of Photochemistry, CAS Research/Education Center for Excellence in Molecular Sciences, Institute of Chemistry, Chinese Academy of Sciences, Beijing 100190, China; University of Chinese Academy of Sciences, Beijing 100049, China*

Hongwei Ji − *Key Laboratory of Photochemistry, CAS Research/Education Center for Excellence in Molecular Sciences, Institute of Chemistry, Chinese Academy of Sciences, Beijing 100190, China; University of Chinese Academy of Sciences, Beijing 100049, China*

Jincai Zhao − *Key Laboratory of Photochemistry, CAS Research/Education Center for Excellence in Molecular Sciences, Institute of Chemistry, Chinese Academy of Sciences, Beijing 100190, China; University of Chinese Academy of Sciences, Beijing 100049, China;* orcid.org/0000-0003-1449-4235

Complete contact information is available at: https://pubs.acs.org/10.1021/acssensors.4c02133

Author Contributions

‖C.L., X.C., and Y.G. contributed equally to this work.

Notes

The authors declare no competing financial interest.

ACKNOWLEDGMENTS

We thank the National Key Research and Development Program of China (No. 2022YFA1205501, 2019YFA0210401) and the Strategic Priority Research Program of Chinese Academy of Sciences (Grant No. XDB36000000); funding: NSFC (Nos. 21925604, 22321004).

REFERENCES

(1) Koner, K.; Karak, S.; Kandambeth, S.; Karak, S.; Thomas, N.; Leanza, L.; Perego, C.; Pesce, L.; Capelli, R.; Moun, M.; Bhakar, M.; Ajithkumar, T. G.; Pavan, G. M.; Banerjee, R. Porous covalent organic nanotubes and their assembly in loops and toroids. *Nat. Chem.* **2022**, *14* (5), 507−514.

(2) Shimizu, T.; Ding, W.; Kameta, N. Soft-Matter Nanotubes: A Platform for Diverse Functions and Applications. *Chem. Rev.* **2020**, *120* (4), 2347−2407.

(3) Valera, J. S.; Arima, H.; Naranjo, C.; Saito, T.; Suda, N.; Gómez, R.; Yagai, S.; Sánchez, L. Biasing the Hierarchy Motifs of Nanotoroids: from 1D Nanotubes to 2D Porous Networks. *Angew. Chem., Int. Ed.* **2022**, *61* (5), No. e202114290.

(4) Sun, M.; Lee, M. Switchable Aromatic Nanopore Structures: Functions and Applications. *Acc. Chem. Res.* **2021**, *54* (14), 2959−2968.

(5) Tan, L.; Sun, M.; Wang, H.; Wang, J.; Kim, J.; Lee, M. Enantiocontrolled macrocyclization by encapsulation of substrates in chiral capsules. *Nat. Synth.* **2023**, *2* (12), 1222−1231.

(6) Sun, B.; Kim, Y.; Wang, Y.; Wang, H.; Kim, J.; Liu, X.; Lee, M. Homochiral porous nanosheets for enantiomer sieving. *Nat. Mater.* **2018**, *17* (7), 599−604.

(7) Gorecka, E.; Vaupotič, N.; Zep, A.; Pociecha, D. From Sponges to Nanotubes: A Change of Nanocrystal Morphology for Acute-Angle Bent-Core Molecules. *Angew. Chem., Int. Ed.* **2016**, *55* (40), 12238−12242.

(8) Albacete, P.; Martínez, J. I.; Li, X.; López-Moreno, A.; Mena-Hernando, Sa.; Platero-Prats, A. E.; Montoro, C.; Loh, K. P.; Pérez, E. M.; Zamora, F. Layer-Stacking-Driven Fluorescence in a Two-Dimensional Imine-Linked Covalent Organic Framework. *J. Am. Chem. Soc.* **2018**, *140* (40), 12922−12929.

(9) Zhang, L.; Yi, L.; Sun, Z.-J.; Deng, H. Covalent organic frameworks for optical applications. *Aggregate* **2021**, *2* (3), No. e24.

(10) Bösch, C. D.; Langenegger, S. M.; Häner, R. Light-Harvesting Nanotubes Formed by Supramolecular Assembly of Aromatic Oligophosphates. *Angew. Chem., Int. Ed.* **2016**, *55* (34), 9961−9964.

(11) Dalapati, S.; Jin, E.; Addicoat, M.; Heine, T.; Jiang, D. Highly Emissive Covalent Organic Frameworks. *J. Am. Chem. Soc.* **2016**, *138* (18), 5797−5800.

(12) Prasanthkumar, S.; Zhang, W.; Jin, W.; Fukushima, T.; Aida, T. Selective Synthesis of Single- and Multi-Walled Supramolecular Nanotubes by Using Solvophobic/Solvophilic Controls: Stepwise Radial Growth via "Coil-on-Tube" Intermediates. *Angew. Chem., Int. Ed.* **2015**, *54* (38), 11168−11172.
(13) Ma, X.; Zhang, Y.; Zhang, Y.; Liu, Y.; Che, Y.; Zhao, J. Fabrication of Chiral-Selective Nanotubular Heterojunctions through Living Supramolecular Polymerization. *Angew. Chem., Int. Ed.* **2016**, *55* (33), 9539−9543.
(14) Ma, X.; Zhang, Y.; Zhang, Y.; Peng, C.; Che, Y.; Zhao, J. Stepwise Formation of Photoconductive Nanotubes through a New Top-Down Method. *Adv. Mater.* **2015**, *27* (47), 7746−7751.
(15) Feng, H.-T.; Yuan, Y.-X.; Xiong, J.-B.; Zheng, Y.-S.; Tang, B. Z. Macrocycles and cages based on tetraphenylethylene with aggregation-induced emission effect. *Chem. Soc. Rev.* **2018**, *47* (19), 7452−7476.
(16) Xu, J.; Wang, J.; Bakr, O. M.; Hadjichristidis, N. Controlling the Fluorescence Performance of AIE Polymers by Controlling the Polymer Microstructure. *Angew. Chem., Int. Ed.* **2023**, *62* (12), No. e202217418.
(17) Liu, C.; Wang, X.; Liu, J.; Yue, Q.; Chen, S.; Lam, J. W. Y.; Luo, L.; Tang, B. Z. Near-Infrared AIE Dots with Chemiluminescence for Deep-Tissue Imaging. *Adv. Mater.* **2020**, *32* (43), No. 2004685.
(18) Li, Z.; Jiang, F.; Yu, M.; Li, S.; Chen, L.; Hong, M. Achieving gas pressure-dependent luminescence from an AIEgen-based metal-organic framework. *Nat. Commun.* **2022**, *13* (1), No. 2142.
(19) Liu, C.-Y.; Chen, X.-R.; Chen, H.-X.; Niu, Z.; Hirao, H.; Braunstein, P.; Lang, J.-P. Ultrafast Luminescent Light-Up Guest Detection Based on the Lock of the Host Molecular Vibration. *J. Am. Chem. Soc.* **2020**, *142* (14), 6690−6697.
(20) Zhang, X.; Chen, Z.; Liu, X.; Hanna, S. L.; Wang, X.; Taheri-Ledari, R.; Maleki, A.; Li, P.; Farha, O. K. A historical overview of the activation and porosity of metal−organic frameworks. *Chem. Soc. Rev.* **2020**, *49* (20), 7406−7427.
(21) Liu, Y.; Guan, X.; Fang, Q. Recent advances in AIEgen-based crystalline porous materials for chemical sensing. *Aggregate* **2021**, *2* (3), No. e34.
(22) Zhu, Z.-H.; Ni, Z.; Zou, H.-H.; Feng, G.; Tang, B. Z. Smart Metal−Organic Frameworks with Reversible Luminescence/Magnetic Switch Behavior for HCl Vapor Detection. *Adv. Funct. Mater.* **2021**, *31* (52), No. 2106925.
(23) Dong, J.; Li, X.; Zhang, K.; Di Yuan, Y.; Wang, Y.; Zhai, L.; Liu, G.; Yuan, D.; Jiang, J.; Zhao, D. Confinement of Aggregation-Induced Emission Molecular Rotors in Ultrathin Two-Dimensional Porous Organic Nanosheets for Enhanced Molecular Recognition. *J. Am. Chem. Soc.* **2018**, *140* (11), 4035−4046.
(24) Xiao, F.; Li, Y.; Li, J.; Lei, D.; Wang, G.; Zhang, T.; Hu, X.; Dou, X. A family of oligo(p-phenylenevinylene) derivative aggregation-induced emission probes: Ultrasensitive, rapid, and anti-interfering fluorescent sensing of perchlorate via precise alkyl chain length modulation. *Aggregate* **2023**, *4* (2), No. e260.
(25) Zhang, Q.; Yin, B.; Hao, J.; Ma, L.; Huang, Y.; Shao, X.; Li, C.; Chu, Z.; Yi, C.; Wong, S. H. D.; Yang, M. An AIEgen/graphene oxide nanocomposite (AIEgen@GO)-based two-stage "turn-on" nucleic acid biosensor for rapid detection of SARS-CoV-2 viral sequence. *Aggregate* **2023**, *4* (1), No. e195.
(26) Cui, L. F.; Gong, Y. J.; Cheng, C. Q.; Guo, Y. X.; Xiong, W.; Ji, H. W.; Jiang, L.; Zhao, J. C.; Che, Y. K. Highly Photostable and Luminescent Donor-Acceptor Molecules for Ultrasensitive Detection of Sulfur Mustard. *Adv. Sci.* **2021**, *8* (4), 2002615 DOI: 10.1002/advs.202002615.
(27) Liao, C.; Gong, Y.; Che, Y.; Cui, L.; Liu, Y.; Ji, H.; Zhang, Y.; Zang, L.; Zhao, J.; Che, Y. Living Self-Assembly of Metastable and Stable Two-Dimensional Platelets from a Single Small Molecule. *Chem.—Eur. J.* **2023**, *29*, No. e202301747.
(28) Cui, L. F.; Gong, Y. J.; Yu, X. T.; Lv, C. X.; Du, X. M.; Zhao, J. C.; Che, Y. K. Development of a Fluorophore with Enhanced Unorthodox Chalcogen Bonding for Highly Sensitive Detection of Trimethyl Arsine Vapor. *ACS Sens.* **2021**, *6* (8), 2851−2857.
(29) Huang, Z.; Kang, S.-K.; Banno, M.; Yamaguchi, T.; Lee, D.; Seok, C.; Yashima, E.; Lee, M. Pulsating Tubules from Noncovalent Macrocycles. *Science* **2012**, *337* (6101), 1521−1526.
(30) Xiong, Z.; Gong, W.; Xu, P.; Jiang, M.; Cai, X.; Zhu, Y.; Ping, X.; Feng, H.; Ma, H.; Qian, Z. Reexamining the heavy-atom-effect: The universal heavy-atom-induced fluorescence enhancement principle for through-space conjugated AIEgens. *Chem. Eng. J.* **2023**, *451*, No. 139030.
(31) Lower, S. K.; El-Sayed, M. A. The Triplet State and Molecular Electronic Processes in Organic Molecules. *Chem. Rev.* **1966**, *66* (2), 199−241.
(32) Nsubuga, L.; Duggen, L.; Balzer, F.; Høegh, S.; Marcondes, T. L.; Greenbank, W.; Rubahn, H.-G.; de Oliveira Hansen, R. Modeling Nonlinear Dynamics of Functionalization Layers: Enhancing Gas Sensor Sensitivity for Piezoelectrically Driven Microcantilever. *ACS Sens.* **2024**, *9* (4), 1842−1856.
(33) Zhang, Q.; Yu, L.; Han, W.; Yang, L.; Li, H.; Sun, S.; Xu, Y. A Self-Calibrating Sensing Platform Based on Amine-Responsive Excitation Wavelength-Dependent Fluorescent Polymers for Real-Time and Visual Detection of Food Freshness. *Adv. Funct. Mater.* **2024**, No. 2410000.
(34) Andre, R. S.; Schneider, R.; DeLima, G. R.; Fugikawa-Santos, L.; Correa, D. S. Wireless Sensor for Meat Freshness Assessment Based on Radio Frequency Communication. *ACS Sens.* **2024**, *9* (2), 631−637.
(35) Ye, H.; Koo, S.; Beitong, Z.; Ke, Y.; Sheng, R.; Duan, T.; Zeng, L.; Kim, J. S. Real-Time Fluorescence Screening Platform for Meat Freshness. *Anal. Chem.* **2022**, *94* (44), 15423−15432.
(36) Sun, L.; Rotaru, A.; Garcia, Y. A non-porous Fe(II) complex for the colorimetric detection of hazardous gases and the monitoring of meat freshness. *J. Hazard. Mater.* **2022**, *437*, No. 129364.
(37) Kim, H.; Trinh, B. T.; Kim, K. H.; Moon, J.; Kang, H.; Jo, K.; Akter, R.; Jeong, J.; Lim, E.-K.; Jung, J.; Choi, H.-S.; Park, H. G.; Kwon, O. S.; Yoon, I.; Kang, T. Au@ZIF-8 SERS paper for food spoilage detection. *Biosens. Bioelectron.* **2021**, *179*, No. 113063.
(38) Quan, Z.; He, H.; Zhou, H.; Liang, Y.; Wang, L.; Tian, S.; Zhu, H.; Wang, S. Designing an intelligent nanofiber ratiometric fluorescent sensor sensitive to biogenic amines for detecting the freshness of shrimp and pork. *Sens. Actuators, B* **2021**, *333*, No. 129535.
(39) Jia, R.; Tian, W.; Bai, H.; Zhang, J.; Wang, S.; Zhang, J. Amine-responsive cellulose-based ratiometric fluorescent materials for real-time and visual detection of shrimp and crab freshness. *Nat. Commun.* **2019**, *10* (1), No. 795.
(40) Hu, Y.; Ma, X.; Zhang, Y.; Che, Y.; Zhao, J. Detection of Amines with Fluorescent Nanotubes: Applications in the Assessment of Meat Spoilage. *ACS Sens.* **2016**, *1* (1), 22−25.
(41) Li, Z.; Suslick, K. S. Portable Optoelectronic Nose for Monitoring Meat Freshness. *ACS Sens.* **2016**, *1* (11), 1330−1335.
(42) Liu, S. F.; Petty, A. R.; Sazama, G. T.; Swager, T. M. Single-Walled Carbon Nanotube/Metalloporphyrin Composites for the Chemiresistive Detection of Amines and Meat Spoilage. *Angew. Chem., Int. Ed.* **2015**, *54* (22), 6554−6557.
(43) Andre, R. S.; Mercante, L. A.; Facure, M. H. M.; Sanfelice, R. C.; Fugikawa-Santos, L.; Swager, T. M.; Correa, D. S. Recent Progress in Amine Gas Sensors for Food Quality Monitoring: Novel Architectures for Sensing Materials and Systems. *ACS Sens.* **2022**, *7* (8), 2104−2131.
(44) Yu, X. T.; Gong, Y. J.; Ji, H. W.; Cheng, C. Q.; Lv, C. X.; Zhang, Y. F.; Zang, L.; Zhao, J. C.; Che, Y. K. Rapid Assessment of Meat Freshness by the Differential Sensing of Organic Sulfides Emitted during Spoilage. *ACS Sens.* **2022**, *7* (5), 1395−1402.
(45) Cox, J. R.; Müller, P.; Swager, T. M. Interrupted Energy Transfer: Highly Selective Detection of Cyclic Ketones in the Vapor Phase. *J. Am. Chem. Soc.* **2011**, *133* (33), 12910−12913.

https://doi.org/10.1021/acssensors.4c02133
ACS Sens. 2024, 9, 6228−6235